

Formation of the Enhanced-V Infrared Cloud-Top Feature from High-Resolution Three-Dimensional Radar Observations

CAMERON R. HOMEYER

National Center for Atmospheric Research, Boulder, Colorado*

(Manuscript received 7 March 2013, in final form 11 July 2013)

ABSTRACT

The responsible mechanism for the formation of the enhanced-V infrared cloud-top feature observed above tropopause-penetrating thunderstorms is not well understood. A new method for the combination of volumetric radar reflectivity from individual radars into three-dimensional composites with high vertical resolution (1 km) is introduced and used to test various formation mechanisms proposed in the literature. For analysis, a set of 89 enhanced-V storms over the eastern continental United States are identified in the 10-yr period from 2001 to 2010 using geostationary satellite data. The background atmospheric state from each storm is determined using the Interim ECMWF Re-Analysis (ERA-Interim) and radiosonde observations. In conjunction with the infrared temperature fields, analysis of the radar data in a coordinate relative to the location of the overshooting convective top and in altitudes relative to the tropopause suggests that above-anvil (stratospheric) cirrus clouds are the most likely mechanism for the formation of the enhanced V.

1. Introduction

Early studies of enhanced longwave infrared (IR) satellite imagery identified a distinct cold “V” feature at the cloud top of some tropopause-penetrating thunderstorms (e.g., Adler et al. 1981; Fujita 1982; Negri 1982). This so-called enhanced V is characterized by a distinct warm region in the storm anvil that is bounded by colder IR temperatures above the overshooting top upstream and outward in the direction of the anvil boundaries downstream, forming a cold V, U, or even ring feature around the warmer anvil region. An illustration of this feature as observed in enhanced IR imagery is given in Fig. 1a. Several studies have linked the enhanced V to severe thunderstorms and its usefulness as a predictor of severe weather has been explored (e.g., McCann 1983; Adler et al. 1985; Brunner et al. 2007). The responsible mechanism for the formation of the enhanced V, however, is not well understood.

Various explanations for the formation of the enhanced V have been proposed in the literature. One hypothesis suggests that the colder V branches are formed by the erosion of the overshooting top and advection downstream by the environmental wind, while subsidence of stratospheric air in the wake of the overshooting top lowers, mixes with, and warms the anvil region (e.g., Heymsfield et al. 1983a; Heymsfield and Blackmer 1988). Warming could also be attained in the absence of mixing if the cloud top in the wake of the updraft subsides to altitudes below the surrounding anvil and the tropopause (e.g., McCann 1983; Heymsfield et al. 1991). An illustration of both subsidence-driven characteristics is given in Fig. 1b.

An additional explanation for the formation of the enhanced V suggests that the warm anvil region is the result of a cirrus cloud layer at altitudes above the storm anvil emitting at warmer stratospheric temperatures and partially masking the colder anvil region below (e.g., Fujita 1982). An illustration of this formation mechanism is given in Fig. 1c. These stratospheric cirrus clouds have been observed above the anvils of deep convective storms from satellite in both stereoscopic height fields and multispectral IR analysis, and from aircraft with visible imagery and polarization lidar (e.g., Fujita 1982; Adler et al. 1983; Mack et al. 1983; Spinhirne et al. 1983; Setvák and Doswell 1991; Levizzani and

*The National Center for Atmospheric Research is sponsored by the National Science Foundation.

Corresponding author address: Cameron Homeyer, National Center for Atmospheric Research, 1850 Table Mesa Dr., P.O. Box 3000, Boulder, CO 80305.
E-mail: chomeyer@ucar.edu

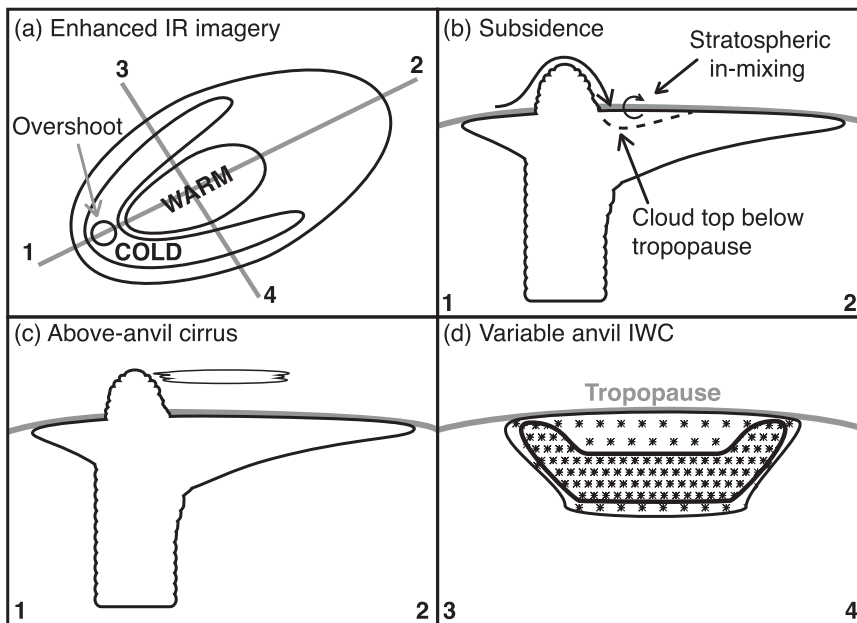


FIG. 1. Illustrations of (a) the observed enhanced-V feature in IR imagery and storm characteristics consistent with the proposed formation mechanisms of (b) subsidence downstream of the overshooting top, (c) above-anvil cirrus clouds, and (d) variable anvil IWC.

Setvák 1996). More recently, the first documented enhanced-V case observed by high-resolution space-based lidar observations also illustrates the presence of above-anvil cirrus cloud within the enclosed warm anvil region (Setvák et al. 2013). There are two potential sources for stratospheric cirrus identified in the literature. The first source is from the lofting of anvil material (“jumping cirrus”) immediately downstream of the overshooting top via gravity wave breaking (Fujita 1982). The second source is from turbulent mixing and downstream transport of the overshooting top itself (Wang 2003). The contribution of each source to the net production of stratospheric cirrus is not known.

There are other explanations for the formation of the enhanced V that have not been evidenced or inferred from observations. These include differences in emissivity between the overshooting top and surrounding anvil (McCann 1983) and variable ice water content (IWC) between the cold V branches and enclosed warm region of the anvil (Heymsfield et al. 1983b). Assuming that the overshooting top is thicker and more emissive than the surrounding anvil and the actual temperature over the entire cloud top is uniform, the overshooting top would be observed in the IR at much warmer temperatures than the surrounding anvil. Although emissivity differences are potentially significant for IR observations of overshooting storms in general, these arguments alone do not explain the formation of the enhanced V. In addition, aircraft observations show that observed IR

temperature changes in overshooting storms are directly related to changes in altitude and suggest that emissivity differences are often negligible (e.g., Heymsfield et al. 1991). Variable IWC in the anvil region follows the argument for erosion of the overshooting top and advection of hydrometeors and cloud particles downstream by the environmental wind, leaving dense convectively lofted ice particles in the enhanced-V branches and less dense particles in the enclosed anvil, allowing the IR imager to penetrate to lower altitudes and sense warmer tropospheric temperatures. An illustration of variable anvil IWC as an enhanced-V formation mechanism is given Fig. 1d.

An interesting feature of enhanced-V storms is that the coldest IR temperatures are often observed immediately upstream of the maximum overshoot altitude (e.g., Heymsfield et al. 1983a). This alignment of the temperature gradient and maximum overshoot altitude would suggest that subsidence may not be responsible for the observed warming, since downward motion is assumed to be strongest in the wake of the overshooting top. To identify the responsible mechanism for warming, various modeling approaches have been applied to enhanced-V storms in the literature. Simple idealized models do illustrate the potential for subsidence warming at the cloud top downstream of the overshoot (e.g., Adler and Mack 1986; Lin 1986; Schlesinger 1990). These models also illustrate that the observed offset between the maximum overshoot

altitude and minimum IR temperature can be obtained by simply introducing a strong temperature inversion above the tropopause. A limitation of the idealized models, however, is that they do not resolve the full thermodynamics, microphysics, and three-dimensional structure of the storm. Recent three-dimensional model analyses of tropopause-penetrating storms have suggested that turbulent mixing and gravity wave breaking near the overshooting top can transport large amounts of water vapor and cirrus cloud deep into the lower stratosphere (e.g., Wang 2003; Luderer et al. 2007; Setvák et al. 2010). These complex, state-of-the-art simulations provide increasing support for stratospheric cirrus, rather than subsidence, as the responsible mechanism for the formation of an enclosed warm anvil region. As a result, further observational evidence of enhanced-V storms is needed to validate the model results.

In this study, formation mechanisms for the enhanced V are tested using radar observations from the Next Generation Weather Radar (NEXRAD) program Weather Surveillance Radar-1988 Doppler (WSR-88D) network (Crum and Alberty 1993). A novel approach for the combination of reflectivity data from several radars to produce high-resolution, three-dimensional reflectivity fields with altitude uncertainties less than 1 km is introduced. These composite radar fields are obtained for a set of discrete tropopause-penetrating storms with enhanced-V IR features identified in the 10-yr period from 2001 to 2010. A composite analysis of the vertical extent of each storm is contrasted with the IR temperature fields in a coordinate system relative to the location of the overshooting top. Because the WSR-88D observations are not capable of observing cloud particles smaller than precipitable hydrometeors, direct observation of stratospheric cirrus clouds is not possible. The low uncertainty in radar reflectivity altitude and high vertical sampling, however, allow for the examination of subsidence warming and variable anvil IWC as potential enhanced-V formation mechanisms.

2. Data and methods

a. ERA-Interim data

The global atmospheric Interim European Centre for Medium-Range Weather Forecasts (ECMWF) Re-Analysis (ERA-Interim) is used for atmospheric temperatures, winds, and tropopause altitudes (Dee et al. 2011). Reanalyses are provided daily at 0000, 0600, 1200, and 1800 UTC on a horizontal Gaussian grid with a longitude–latitude resolution of $0.75^\circ \times \sim 0.75^\circ$ (~ 80 km) and 37 unevenly spaced pressure levels in the vertical. Meteorological parameters are interpolated linearly in

space and time for analysis. The tropopause is computed by first interpolating the temperature column to higher resolution using cubic splines, followed by the application of the World Meteorological Organization (WMO) definition (World Meteorological Organization 1957) as outlined in Homeyer et al. (2010).

b. Radiosonde data

Radiosonde data from locations operated by the National Weather Service (NWS) are used for comparison with ERA-Interim fields. The radiosondes are typically available twice daily at 0000 and 1200 UTC, and sometimes at 0600 or 1800 UTC for severe or significant weather conditions. The vertical resolution of each profile is about 30 m.

c. GOES data

IR imagery from the National Oceanic and Atmospheric Administration (NOAA) Geostationary Operational Environmental Satellite (GOES) system is used for cloud-top temperature and enhanced-V identification (Menzel and Purdom 1994). Full disc scans are completed in ~ 26 min and provided every 3 h starting at about 0000 UTC by NOAA through the Comprehensive Large Array-data Stewardship System (CLASS). Two operational GOES continuously monitor the weather over the Continental United States: GOES-East and GOES-West. GOES-West is stationed over the western coast of the United States at 135° W longitude, and GOES-East over the east coast at 75° W longitude. The IR imager aboard the GOES has a horizontal resolution of 4 km at nadir and an absolute accuracy of ≤ 1 K. Brightness temperatures are computed using the channel-4 wavelength band (10.2 – $11.2 \mu\text{m}$). All available 3-hourly full disc scans from the GOES-East (*GOES-8*, *-12*, and *-13*) imagers are used for analysis. GOES-West (*GOES-10* and *-11*) scans are supplemented in the case of missing or incomplete GOES-East disc images. For analysis, the continental United States region is extracted from each full disc and re-gridded to a regular 0.02° (~ 2 km) longitude–latitude grid using a Delaunay triangulation.

d. NEXRAD WSR-88D data

Three-dimensional data from NEXRAD WSR-88Ds is provided by the National Climatic Data Center (NCDC) on native spherical grids. The spatial and temporal resolution of the data varies depending on year, meteorology, operating status, and range from the radar. For convective systems, scans are completed at 14 elevations in the vertical with the typical time between volume scans of 4–7 min. For data prior to May 2008, volume information is stored at a resolution of 1° in

azimuth and 1 km in range from the radar. Following the completion of system upgrades to support higher-resolution volume scans in August 2008, data for all radars is available at a resolution of 0.5° in azimuth and 0.25 km in range.

The maximum unambiguous range of the WSR-88Ds varies depending on the variable observed. Doppler velocities are only observable out to 230 km in range for the older, low-resolution data and out to 300 km in range for the newer, high-resolution volume scans. For reflectivity data, the radar can observe hydrometeors out to 460 km in range for both resolutions. In addition, variables are consistently available at altitudes below ~ 25 km. The WSR-88Ds are capable of sensing reflectivities well below the scale of dense precipitable hydrometeors, especially at close ranges from the radar. The minimum detectable signal of the radar is -42 dBZ at 1 km and increases with increasing range to about 11 dBZ at the maximum detectable range of 460 km (Crum and Alberty 1993). This limitation is important to consider when evaluating the intensity and extent of a given storm. The characteristics of beam coverage also limit the analysis of storms at distant ranges from a single radar. Because the WSR-88D beam is conical with an angular beamwidth of 0.95° , there is inherent increasing spatial coverage of the beam with increasing range. In addition, individual scan altitudes increase with increasing range, reducing the number of beams remaining in the troposphere at farther ranges.

WSR-88Ds employ various scan strategies, or Volume Coverage Patterns (VCPs), depending on the presence and type of precipitation. For deep convection, two scan strategies are common: VCP-11 and VCP-12. The VCP-11 strategy has slightly better volume coverage than VCP-12. Figure 2a shows the altitude and depth of each radar beam in VCP-11 as a function of increasing range from the radar. As previously outlined, the increasing depth of individual radar beams with increasing range is determined by the angular width of the transmitted beam. In addition, because each observation corresponds to a finite volume, the range resolution of the beam introduces additional depth to the measurement (up to ~ 375 m). Within 60 km of the radar the vertical depth of each beam is generally less than 1 km while the vertical depth at 300 km from the radar is near 5 km, viewing a much larger portion of the atmosphere. The increasing horizontal extent of the beam is comparable. The decreasing number of scans remaining in the troposphere at distant ranges is clearly illustrated in Fig. 2a, with only three remaining below 20 km in altitude at a range of 300 km. A unique characteristic of the WSR-88D network, however, is the large number and density of radars over

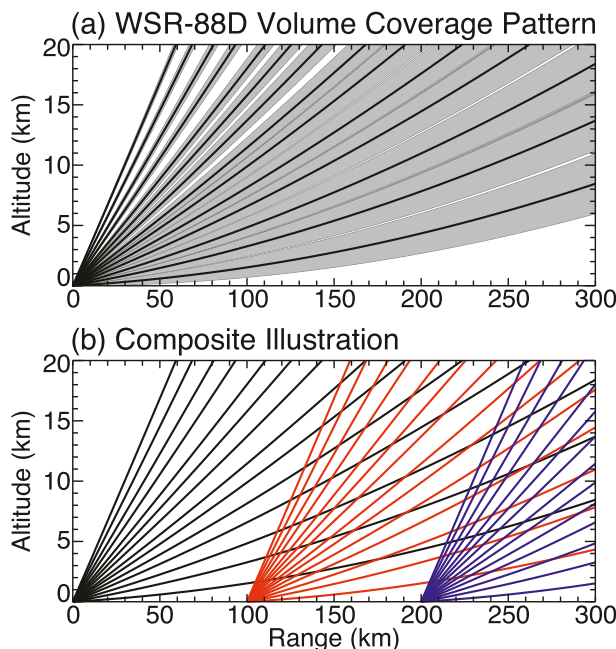


FIG. 2. (a) Beam altitude as a function of range from a radar for the VCP-11 convective scan strategy used for WSR-88Ds and (b) an illustration of the dense vertical sampling attained from a combination of radars that sample the same location at different ranges. The gray color-filled regions in (a) illustrate the increasing depth of the WSR-88D beam with increasing range.

a very large portion of the country. This network of radars allows for the observation of a given atmospheric column by several different systems at varying ranges that, when combined, can provide dense vertical sampling. The effect of such an arrangement is illustrated in Fig. 2b. In this example, three radars operating in convective VCPs observe the the same atmospheric column at a range of 250 km with 25 individual beams below 20 km in altitude.

Three-dimensional compositing of radar data has been explored in the literature to facilitate the improvement of quantitative precipitation estimates, real-time forecasting, and model simulations (e.g., Zhang et al. 2005; Lakshmanan et al. 2006; Langston et al. 2007; Ruzanski and Chandrasekar 2012). In principle, all of these studies combine individual radar observations using the same regridding technique. Individual volume scans are first gridded onto a common three-dimensional Cartesian output domain and then combined using a variety of selecting and averaging algorithms, often involving distance weighting of the observations in range to account for variability in the spatial resolution of the beam. The primary goal of such an approach is to retain spatial scales that are adequately sampled from one radar while preventing retention of corresponding observations from additional radars that are

undersampled (e.g., Trapp and Doswell 2000). One limitation of this approach, however, is the potentially large error in altitude introduced by the application of interpolation to coarse vertical observations prior to compositing. Because the beam altitudes at distant ranges from a radar can be separated by and span depths >3 km, the uncertainty in the vertical extent of an observed storm is often >3 km. In this study, an approach similar to that for regridding observations in the horizontal is applied to each elevation angle in a volume to preserve the native altitudes. These regularly spaced conical gridded data for multiple radars are then combined to create reflectivity fields that are densely sampled in the vertical dimension. The techniques for three-dimensional combination are described in detail in the remaining parts of this section.

For analysis of enhanced-V storms, composite reflectivity fields are made at 5-min intervals within a ± 30 -min time window of the central time of each GOES full disc scan. After horizontal regridding to a regular 0.02° (~ 2 km) longitude–latitude grid, volume data from each radar are first linearly interpolated to uniform times using the two neighboring volume scans. This time interpolation does not take into account storm motion, which is observed to have a negligible impact on the vertical extent of a storm when the time between volume scans is less than 7 min (not shown). The central time of each volume scan is used as the reference time for interpolation. Three-dimensional combination of the radar data at uniform times is accomplished by sorting the native altitudes of contributing radar beams in each grid column. Following combination, the three-dimensional composites are output on a regular vertical grid with 1 km resolution using linear interpolation. Assuming all radars in the WSR-88D network are operating in convective mode, the number of systems contributing to each column and the resulting vertical sampling below 20 km in altitude are shown in Figs. 3a and 3b, respectively. For most of the eastern United States, the network is very dense with at least four radars observing each column of the atmosphere. In addition, the resulting vertical sampling in the troposphere and lower stratosphere from the dense network of beams is better than 1 km for most of the domain. In general, if at least three radars observe a column the vertical sampling is ≤ 1 km. To further illustrate the observational gain from combining all available systems into each column, the mean vertical sampling interval as a function of altitude for the composite domain in Figs. 3a and 3b and for that averaged over the entire domain of a single radar (out to 300 km) is given in Fig. 4. If only one radar is used for analysis, the vertical sampling interval is larger than 3 km at an altitude of 20 km while the

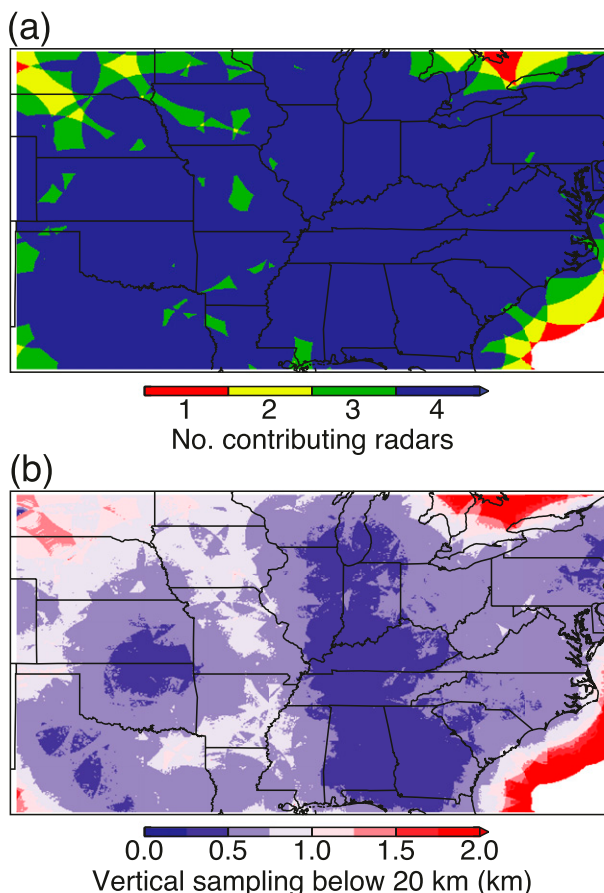


FIG. 3. For the three-dimensional WSR-88D composite: maps of (a) the number of radars contributing to the vertical column and (b) the mean vertical sampling interval below 20 km in altitude. These maps are generated using the scan strategy shown in Fig. 2a out to 300 km from each radar.

vertical sampling interval for the combined radar product is less than 1 km at all altitudes below 20 km.

As outlined above, the minimum detectable reflectivity signal increases as a function of range from the radar. At 300 km, the maximum range used for the combination method, the minimum detectable signal is ~ 7.5 dBZ. As a result, a reflectivity threshold of 10 dBZ is used for analysis of the extent of observed storms in this study. In addition to detection limits, equal weighting of column observations from distant and near radar systems may potentially introduce reflectivity biases that manifest as biases in the altitude of observed storms. For example, observations from both near and distant radars in the same grid column may share similar central beam altitudes while measuring significantly different depths of the atmosphere. These differences in the observed depth of a storm may result in large differences in the magnitude of observed reflectivity. Further consideration of more complicated

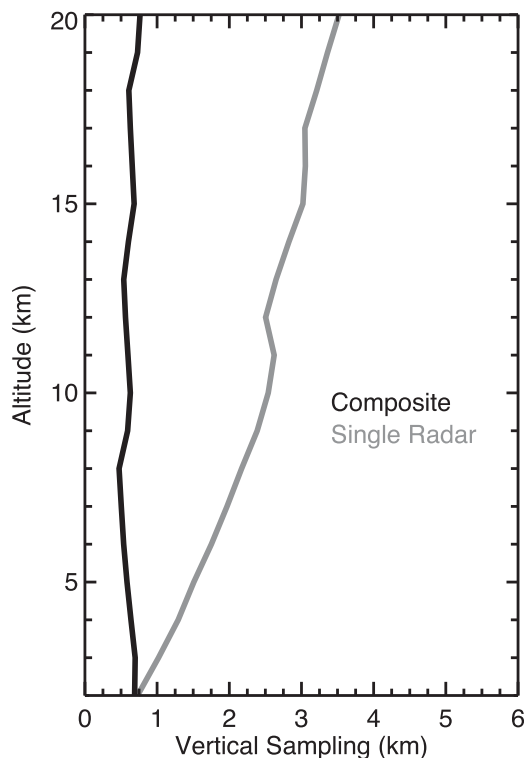


FIG. 4. The mean vertical sampling interval as a function of altitude for the WSR-88D composite in the domain of Fig. 3 and for the nearest 300 km of a single radar.

radar combination techniques such as distance-weighted means would be required to reduce uncertainties in reflectivity and the inferred altitude of a storm (e.g., Trapp and Doswell 2000; Zhang et al. 2005). To test the dependence of reflectivity measurements on the depth of the WSR-88D beam, point comparisons of beams from near and distant radars that share the same central time and nearly intersect, having altitude differences of less than 100 m, are made for all radar observations used in this study. A radar is designated as near if an observation is made with a beam depth of <1 km and designated as distant if made with a beam depth ≥ 3 km. The number of point comparisons acquired for this analysis is $>157\,000$ from 60 unique radar system pairs. Figures 5a and 5b show normalized joint frequency distributions of distant and near observed radar reflectivity and differences between distant and near observations as a function of altitude, respectively. Observed reflectivity magnitudes from distant radars compare well with observations from near radars, generally following a one-to-one relationship with rms differences of 6.95 dBZ. In addition to reflectivity differences, measurements at lower reflectivity and higher altitudes show a slight high bias of 2–3 dBZ for distant radar observations. For all of the radar data analyzed in this study,

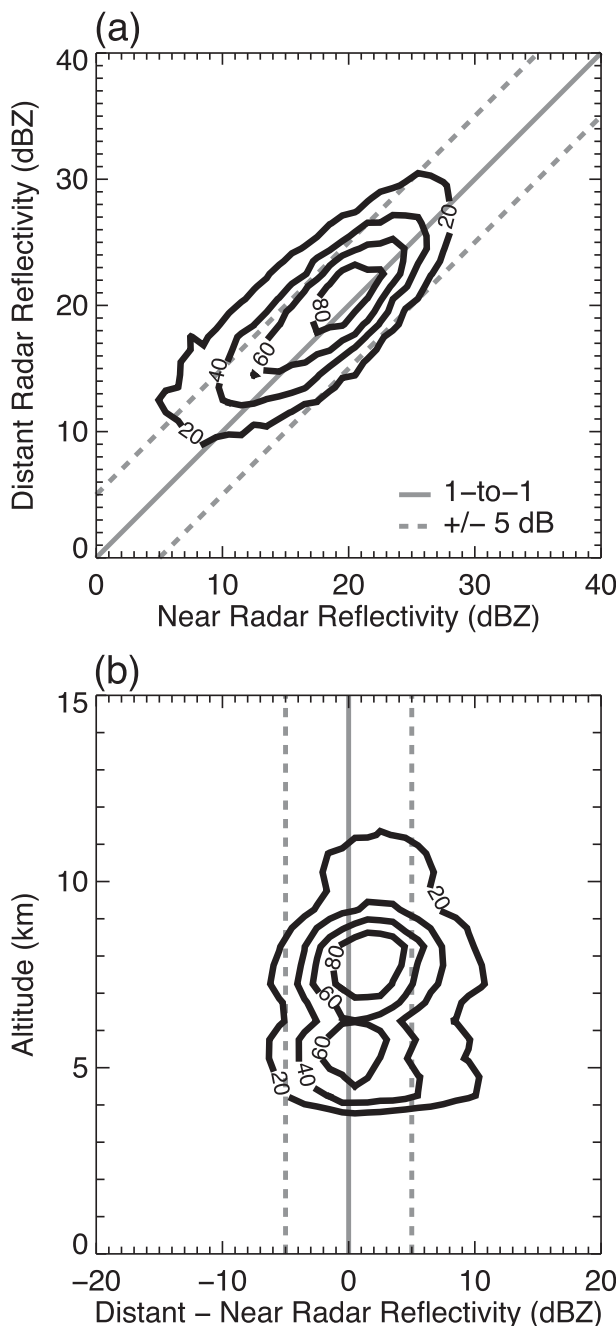


FIG. 5. Normalized joint frequency distributions of WSR-88D (a) reflectivity observed at distant and near radar locations and (b) distant minus near reflectivity differences as a function of altitude. Contributing observations from radar system pairs are at equivalent scan times and within 100 m in altitude of each other. A near radar observation has a beam depth of <1 km; while a distant radar observation has a beam depth ≥ 3 km. Contours are in percentage.

a 7-dBZ difference in reflectivity relative to the 10-dBZ threshold used for analysis of the storm extent corresponds to about a 500-m difference in storm top altitude (not shown). This altitude difference is well below the

1-km composite vertical resolution. These comparisons show that simple linear interpolation of the composite vertical grid to a uniform 1-km grid for analysis is sufficient for resolving the extent of the three-dimensional reflectivity field.

Additional errors in the radar reflectivity observed from a given radar are possible when nonstandard beam refraction or sidelobe contamination are present. The altitude of each beam in a radar volume is calculated assuming a standard index of refraction for the atmosphere. Under dry, near-adiabatic conditions in the lower atmosphere, radar beams can refract less than expected and result in underestimation of the vertical extent of a storm. Conversely, overestimation of the vertical extent is possible if the beam refracts more than expected, which is common if there are significant temperature inversions in the tropospheric boundary layer. These errors from nonstandard refraction, however, are typically limited to beams that travel long distances in the boundary layer and are unlikely to be significant for determining the vertical extent of deep convective clouds (e.g., Doviak and Zrnić 1993). Contamination of the radar measurement from beam side lobes is rare at the reflectivities observable by WSR-88D systems. In general, sidelobe contamination is only possible from the first lobe, -27 dBZ below the main lobe power and at 1.2° away from the beam center in all directions (up to 6 km in altitude for ranges within 300 km). In order for sidelobe contamination to be present, the reflectivity of the meteorological signal in the sidelobe must be stronger than the signal in the main lobe by at least the two-way, first-sidelobe isolation (i.e., ≥ 54 dBZ, Office of the Federal Coordinator for Meteorology 2005). At the 10-dBZ threshold used for the vertical extent of storms in this study, sidelobe contamination of a given beam requires that reflectivities within 1.2° of the beam center exceed 64 dBZ. For the events identified and analyzed in the following sections, only 5 storms show reflectivities within 6 km of the tropopause altitude that exceed 64 dBZ, which are limited to ranges within 5 km of the overshooting top.

To illustrate the fidelity of the WSR-88D compositing method for producing representations of the vertical extent of a given convective storm, comparisons of radar reflectivity from the WSR-88D composite and the Cloud Profiling Radar (CPR) aboard the *CloudSat* are performed. The *CloudSat* system is part of the A-Train constellation of satellites, which provide contiguous measurements of cloud properties from various instruments in order to form a better understanding of clouds throughout the troposphere and their role in climate. The *CloudSat* CPR is a nadir-pointing, 94-GHz cloud radar that observes reflectivities

from -28 to ~ 20 dBZ, sensing hydrometeors well below the threshold of 10 dBZ in the WSR-88D composite (Stephens et al. 2002). The resolution of the CPR is 1.7 km alongtrack and 1.3 km crosstrack in the horizontal and 480 m in the vertical, with profiles oversampled at 1.1 km alongtrack and 240 m in the vertical. One limitation of *CloudSat* is that it retrieves measurements along a sun-synchronous orbit, passing over regions at 1330 and 0130 LT, before and after the times of deepest land convection. As a result, *CloudSat* observations of deep convection over the United States are typically limited to nocturnal mesoscale convective systems (MCSs). In addition, the CPR often suffers from significant attenuation (up to 10 dBZ km $^{-1}$), particularly in environments with large liquid water content. To date, no enhanced-V storms have been observed by the *CloudSat* CPR within the WSR-88D study region. A general analysis of the detection of above-tropopause clouds within the study region, however, yields 10 segments through the core of deep convective storms during the entire *CloudSat* record. An example of one of these overpasses is given in Fig. 6. In this example, the *CloudSat* CPR profiled a leading-line trailing-stratiform MCS near the intersecting borders of Arkansas, Tennessee, and Mississippi. Measurements of the vertical extent of the storm from the WSR-88D composite 10-dBZ threshold and the *CloudSat* CPR compare well near the convective elements of the storm, with differences less than ~ 300 m. Larger separations up to ~ 2 km are found throughout the leading anvil and trailing stratiform regions. Despite these differences in the representation of the cloud top, the altitude of the 10-dBZ threshold from both observing systems agrees to within ~ 500 m throughout the MCS. It should be noted here that although representations of the storm top differ significantly away from the convective line, these large differences are likely not comparable for enhanced-V storms. The formation of the anvil/stratiform region in a MCS is primarily driven by the dynamics of the system itself, for which subsidence plays an increasingly important role in limiting the altitude of hydrometeors detectable by WSR-88Ds (e.g., Houze et al. 1989). In an enhanced-V storm, however, the formation of the anvil region is dominated by rapid advection by the environmental wind, which likely reduces potential discrepancies in altitude between large hydrometeors and smaller particles near the cloud top.

e. Enhanced-V identification

Enhanced-V IR features are identified by subjective analysis of 3-hourly GOES IR brightness temperatures over the 10-yr period from 2001 to 2010. The storms identified for analysis are required to be discrete storms

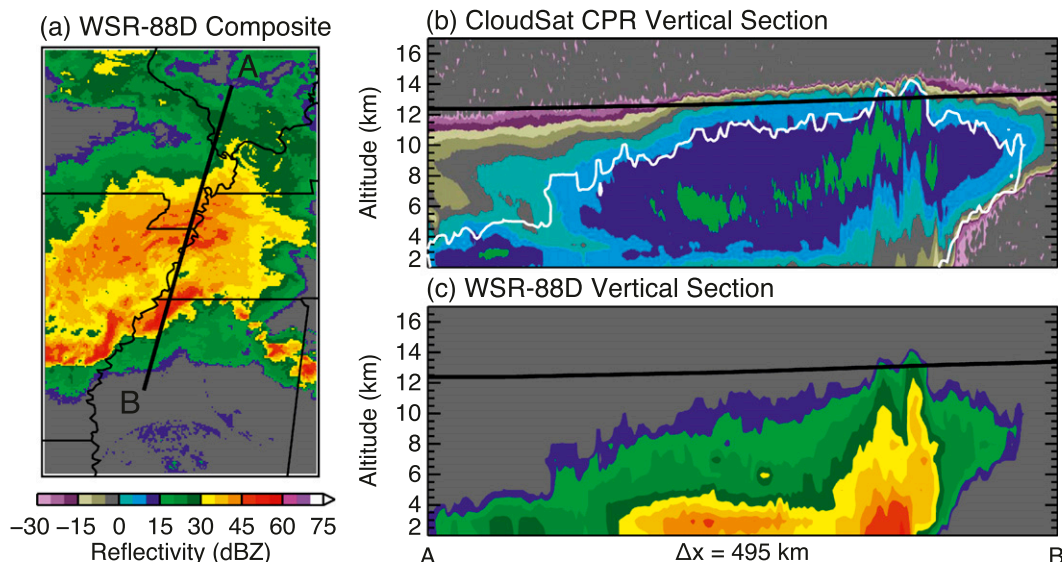


FIG. 6. A comparison of reflectivity observations from the (b) *CloudSat* CPR and (c) WSR-88D composite at 0811 UTC 6 May 2009 through a deep mesoscale convective system near the tropopause. (a) Column-maximum radar reflectivity from the WSR-88D composite and the *CloudSat* path (black line labeled A–B) corresponding to the vertical sections in (b),(c). The ERA-Interim tropopause is shown by the black lines in each vertical section. The white contours in (b) show the 10-dBZ boundary from the WSR-88D composite.

that are not embedded in a MCS. Following the identification of individual storms, radar data are combined following the methods outlined above in section 2d. If radar composites show sufficient vertical coverage in the region of an observed storm (≥ 3 contributing radars), the case is retained for analysis. To test the proposed mechanisms for enhanced-V formation given in the introduction, cross-sections of IR temperatures and radar reflectivity are taken along the apex of the observed V feature and transverse through the warm anvil region enclosed by the cold V branches. For analysis, composites of the identified storms are made relative to the radar and IR-derived overshooting tops.

An example of the cross-sectional analysis of one of the identified storms is given in Fig. 7. Figures 7a and 7b show enhanced IR brightness temperatures and column-maximum radar reflectivity, respectively. The enhanced IR temperature field shows a distinct V feature with an extensive warm region throughout the anvil of the storm. The corresponding radar reflectivity fields are expectedly less extensive than the cloud, but do coincide with the enclosed warm region and outward into the colder V branches. Vertical cross-sections of radar reflectivity along the enhanced-V apex (lines A–B in Figs. 7a and 7b) and transverse (lines C–D) are shown in Figs. 7c and 7d, respectively. The thick black lines near 13 km in each cross section illustrate the altitude of the lapse-rate tropopause from the ERA-Interim. The overshooting convective top is clearly observed in the apex cross

section, reaching altitudes more than 3 km above the unperturbed tropopause. The adjacent storm anvil remains at (or below) the tropopause with downward sloping tops into the increasingly distant anvil, indicative of gradual settling of the larger precipitable hydrometeors. In this example, the radar data show no evidence of warming via below-tropopause subsidence of the anvil immediately downstream of the overshooting top. In addition, the nearly uniform structure of decreasing reflectivity with increasing altitude in the transverse reflectivity section suggests that variations in anvil IWC may not be a responsible mechanism for the enhanced-V feature atop this storm if one assumes an exponential relationship between IWC and radar reflectivity (e.g., Sassen 1987; Liu and Illingworth 2000).

3. Results

The enhanced-V identification techniques outlined in section 2e identify 110 candidate storms. Following three-dimensional compositing of the radar data, 89 storms with sufficient radar coverage are retained for analysis. Figure 8 shows the geographical locations of the contributing storms. The majority of identified storms are concentrated in the Great Plains region of the United States, with the remaining events extending into the northern Midwest. As expected from previous association of the enhanced-V feature with severe weather,

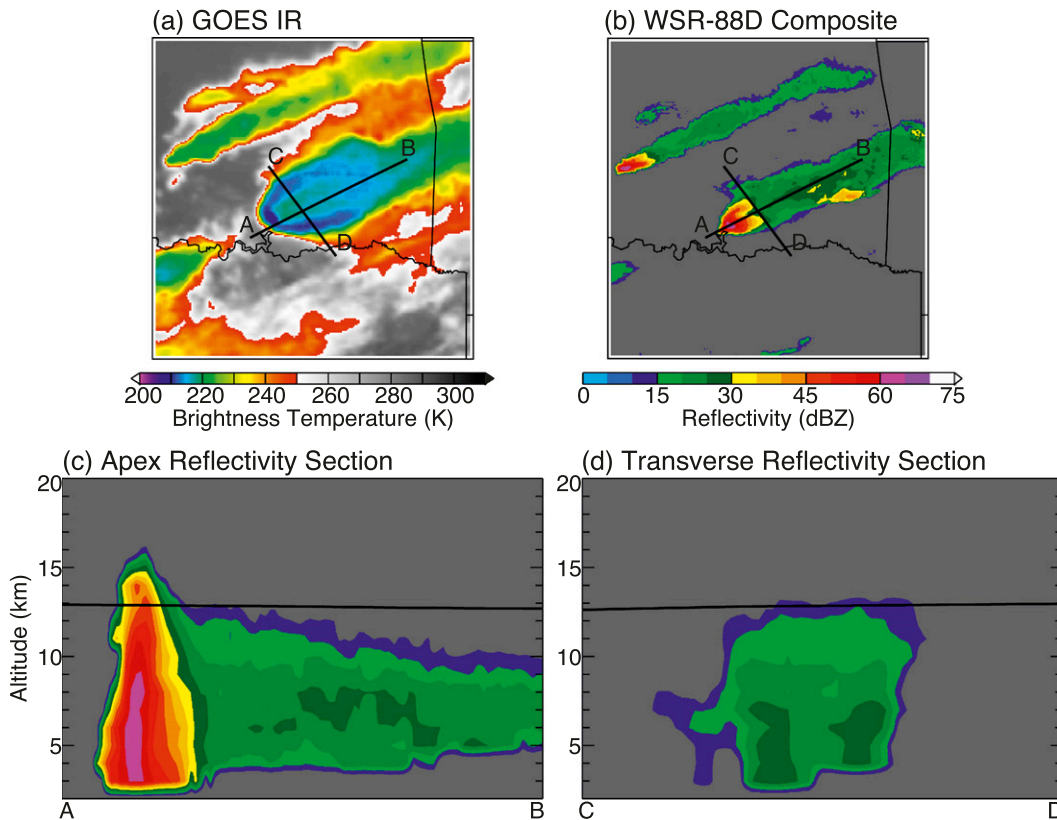


FIG. 7. An example of the methods used for the analysis of enhanced-V storms showing (a) GOES IR brightness temperature, (b) column-maximum radar reflectivity, (c) vertical cross section of radar reflectivity along the line A–B given in (a),(b), and (d) vertical cross section of radar reflectivity along the line C–D given in (a),(b). The observation time for all panels is near 0000 UTC 15 Apr 2001 and the identified storm is located in southeast Oklahoma.

the enhanced-V distribution is similar to that observed for severe storms (e.g., Kelly and Schaefer 1985; Doswell et al. 2005). The annual distribution of these events shows a distinct peak in late spring, also in agreement with known severe storm statistics (see Table 1). In addition, the identified storms are grouped near the time of maximum heating and largest available potential energy for convective storms over the eastern United States (2100–0300 UTC, see Table 2).

The analysis of individual storms relative to the background atmospheric state, such as the tropopause, requires observations that are continuous in time and space. To test the fidelity of the ERA-Interim for reproducing the observed state, NWS radiosonde observations in the upper troposphere and lower stratosphere are compared to reanalysis fields within 300 km of each identified storm. A maximum distance of 300 km from each storm retains 53 individual radiosondes from 49 different storms. Figures 9a–d show comparisons of ERA-Interim and radiosonde tropopause altitudes, and mean profiles of tropopause-relative temperature, wind,

and potential temperature, respectively. The comparisons of tropopause altitudes show that the ERA-Interim and observations agree well, with rms differences of ~ 500 m (the vertical resolution of the reanalysis). The outlying point with a tropopause altitude of ~ 17 km

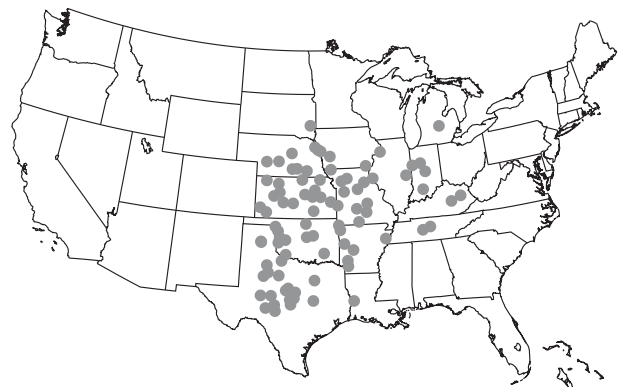


FIG. 8. Locations of the enhanced-V storms analyzed in this study.

TABLE 1. Number of identified enhanced-V storms by month.

Month	Jan	Feb	Mar	Apr	May	Jun	Jul	Aug	Sep	Oct	Nov	Dec
No.	0	2	9	23	37	11	3	3	1	0	0	0

TABLE 2. Number of identified enhanced-V storms by hour.

Hour (UTC)	0000	0300	0600	0900	1200	1500	1800	2100
No.	27	23	12	1	5	4	5	12

from ERA-Interim and ~12 km from radiosonde is a case of misidentification near the sharp jump from extratropical (<13 km) to tropical (>15 km) tropopause heights (e.g., Homeyer et al. 2010). Overestimates in the tropopause height can lead to large underestimates in the relative altitude of an observed storm. Such biases are not observed in the immediate region of the identified storms in this study, as illustrated in the cross-sectional analysis below. Temperature at relative altitude to the tropopause from radiosonde observations shows a strong tropopause inversion layer (TIL)

up to 1–2 km above the tropopause (e.g., Birner 2006). Temperatures from the ERA-Interim are comparable at altitudes >2 km above and >1 km below the tropopause. At the tropopause, however, the ERA-Interim are biased warm by 2–3 K and underestimate the observed TIL. Despite significant biases in temperature near the tropopause, the profiles of potential temperature are nearly indistinguishable. Radiosonde and ERA-Interim wind speeds at relative altitude to the tropopause are comparable, with differences less than 5 m s⁻¹.

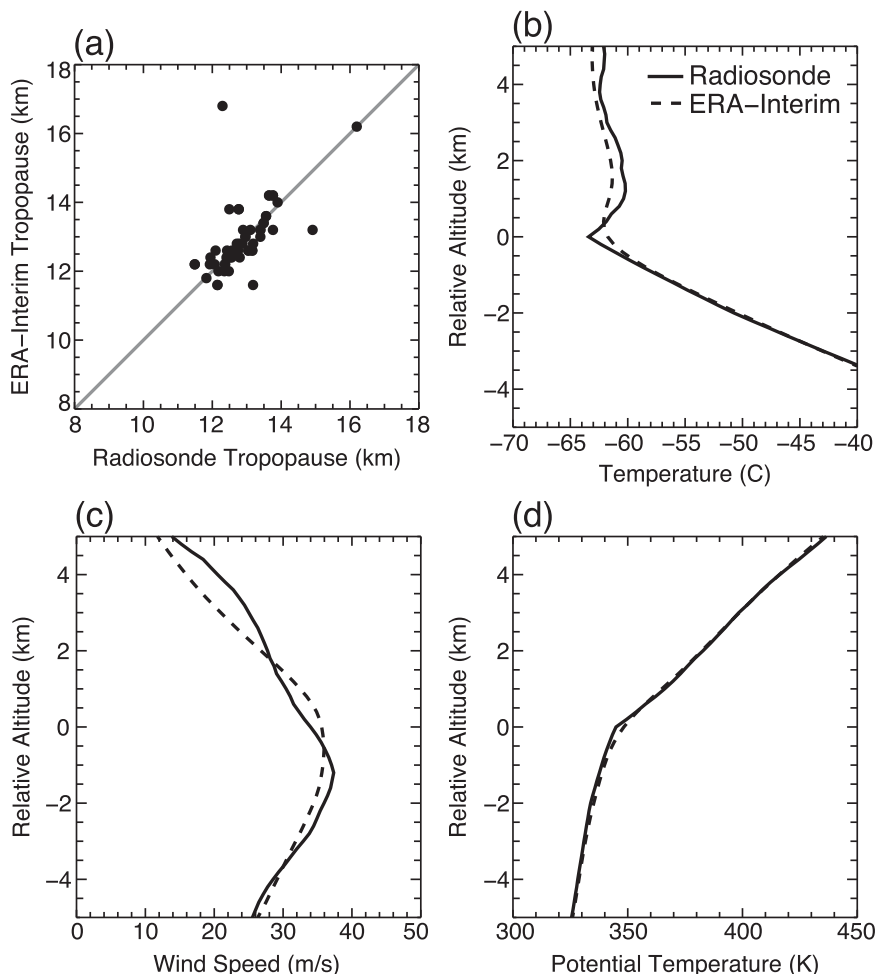


FIG. 9. A comparison of radiosonde and ERA-Interim (a) tropopause altitude, (b) mean temperature at altitudes relative to the tropopause, (c) mean horizontal wind speed at altitudes relative to the tropopause, and (d) mean potential temperature at altitudes relative to the tropopause for profiles within 300 km of an identified storm. ERA-Interim profiles are the dashed lines and radiosonde profiles are the solid lines in (b)–(d).

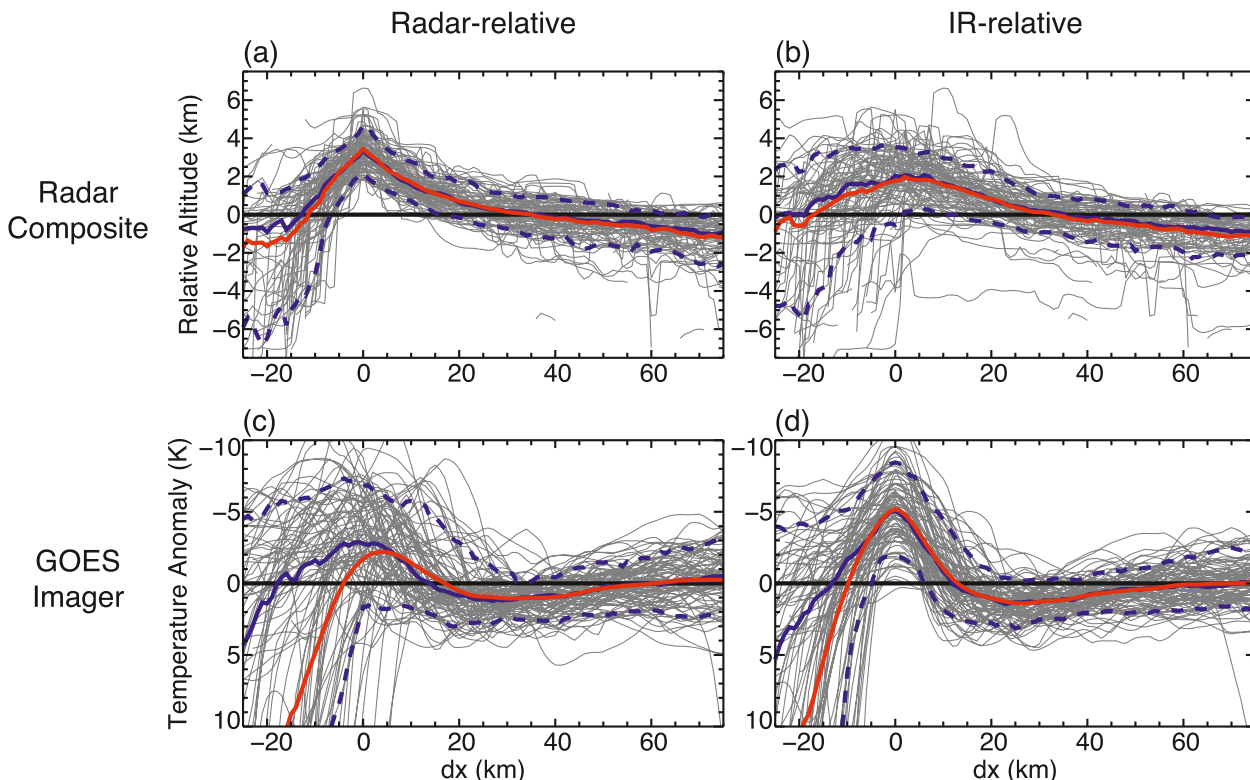


FIG. 10. (a),(b) Composite cross sections of 10-dBZ radar reflectivity altitude relative to the ERA-Interim tropopause and (c),(d) GOES IR brightness temperature anomalies relative to the anvil mean (0–75 km) through the apex of the enhanced V for: (a),(c), relative distance to the maximum 10-dBZ altitude and (b),(d) relative distance to the coldest IR temperature of each storm. The red lines in each panel represent the mean, the blue solid lines represent the median, and the blue dashed lines represent the 10th and 90th percentiles. Relative distance is positive in the direction of the downstream anvil.

Because the altitudes of hydrometeors observed by WSR-88D systems are especially sensitive to motions in both the environment and the storm itself, significant subsidence downstream of the overshooting top should be reflected in the vertical reflectivity distribution, especially along transverse paths through the cold V branches and enclosed warm region of the downstream anvil. Composites of 10-dBZ radar reflectivity altitudes relative to the tropopause and IR brightness temperatures along cross-sections through the apex of the enhanced-V storms (as in Fig. 7c) are given in Fig. 10. GOES IR temperatures are presented as anomalies relative to the mean temperature of the downstream anvil (the overshooting top to 75 km downstream). Figures 10a and 10c show the radar and IR fields in relative distance to the location of the overshooting top as determined from the three-dimensional radar composites. The radar composites show that the typical overshooting depth of enhanced-V storms is ~ 3.5 km above the unperturbed environmental tropopause, ranging from 2 to 5 km. The altitude of the radar-observed storm decreases gradually with increasing distance from the maximum overshoot

altitude, in agreement with the settling of precipitable hydrometeors. The corresponding IR measurements illustrate that the coldest temperatures generally coincide with the maximum overshoot while the warmest temperatures are observed ~ 30 km downwind, becoming slightly colder atop the distant anvil. The large spread in GOES IR measurements in Fig. 10c is likely a combination of slight positioning error, imprecise time-matching of the radar measurements, and the characteristic offset of minimum temperatures and maximum overshoot altitude for enhanced-V storms. To form a better understanding of the typical cold-to-warm temperature fluctuation in the vicinity of the overshooting top, composites relative to the coldest IR temperatures are given in Figs. 10b and 10d. Radar altitudes in an IR-relative coordinate system show greater spread, similar to IR temperatures in the radar-relative coordinate system. Despite the increased spread, the maximum in the composite-mean relative altitude coincides with the location of the minimum IR temperature. The GOES IR temperatures in the IR-relative coordinate are compact and illustrate the sharp temperature change

near the overshooting top. The composite mean in Fig. 10d shows that the typical cold-to-warm temperature change is about 6 K. The warmest temperatures in the IR-relative coordinate are observed 25–30 km downstream, comparable to that shown in the radar-relative coordinate. Comparing Figs. 10a and 10d illustrates that the warmest temperatures do not correspond to storm reflectivity altitudes significantly below the tropopause, in disagreement with strong subsidence downstream of the overshooting top.

To further examine the potential for subsidence warming and variable IWC as enhanced-V formation mechanisms, transverse cross sections through the cold V branches and enclosed warm anvil region are shown in Fig. 11 in relative distance to the intersections with the apex cross sections in Fig. 10. The orientation of the transverse cross section is left to right of the downstream anvil. These transverse sections are taken at 30 km downstream of the maximum radar-overshooting altitude, coincident with the location of the maximum anvil temperature in Fig. 10c. The results for cross sections 30 km downstream of the minimum IR temperature are comparable. Figure 11b clearly illustrates the enclosure of the warm anvil region by the colder V branches. In comparison, tropopause relative altitudes of the 10-dBZ reflectivity surface (Fig. 11a) show a slight swell in altitudes within the warm region, opposite to that expected from subsidence warming. Furthermore, relative altitudes of the 15- and 20-dBZ reflectivity surfaces (dashed and dotted red lines in Fig. 11a) show similar vertical structure. This uniform reflectivity structure suggests that variability in anvil IWC (as illustrated in Fig. 1d) is negligible.

As outlined previously, one limitation of the use of the WSR-88D composite data for identifying the vertical extent of a storm is that it does not observe small cloud particles and can underestimate the true vertical extent. In the region of the overshooting top, the difference between the reflective altitude and cloud top is expected to be small, since large hydrometeors are being lofted within the growing cloud (e.g., see Fig. 6). In the increasingly distant anvil region, however, hydrometeors that are detectable by the radar gradually settle, with the reflective altitudes and cloud top potentially separated by several kilometers. If underestimations of the vertical extent are larger than the depth of subsidence warming downstream of the overshooting top, the resulting variations in altitude would be undetectable by the radar. Heymsfield et al. (1983a) suggest that if airflow past an overshooting top in the stratosphere is analogous to that past a mountain, the magnitude of subsidence warming on the downstream side of the overshoot would depend on the depth of the overshooting

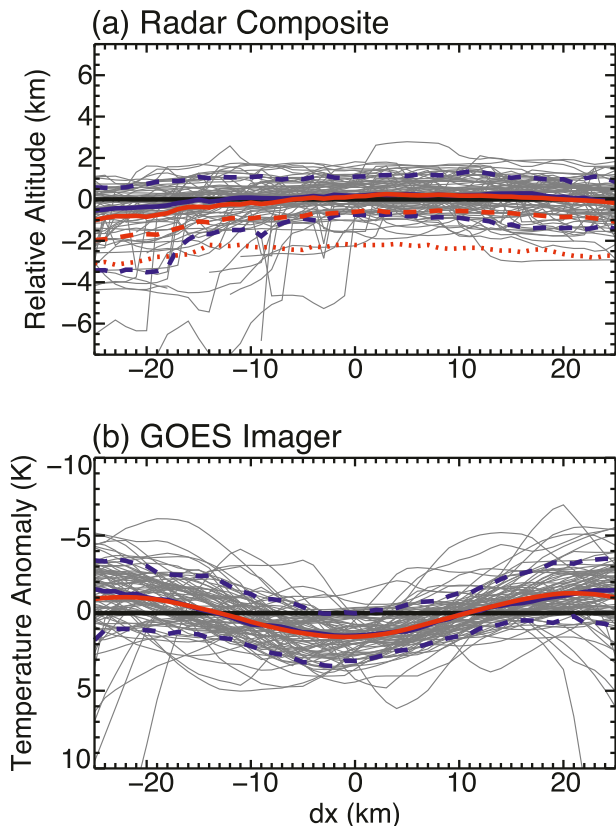


FIG. 11. As in Fig. 10, but for transverse sections through the cold branches and enclosed warm anvil region of the enhanced V: (a) radar composite and (b) GOES imager. Cross sections are taken 30 km downstream of each radar-derived overshoot, coincident with the intersections with the apex cross sections shown in Fig. 10 and oriented left to right of the downstream anvil. The dashed and dotted red lines in (a) show composite-mean relative altitudes of 15- and 20-dBZ radar reflectivities, respectively.

top, the speed of the storm-relative flow, and the stability of the lower stratosphere. These relationships follow the commonly used Froude number for understanding characteristics of flow past an obstacle ($Fr = U/Nz$, where, for the current application, U is the storm-relative wind, N is the static stability, and z is the depth of the overshooting top). For $Fr < 1$, air moves horizontally past an obstacle, while for $Fr > 1$, air moves over the obstacle (i.e., subsidence downstream becomes likely). The radiosonde observations illustrate that the lower-stratospheric stability is similar for the identified storms, with a strong inversion up to 1–2 km above the tropopause (see Fig. 9b). Further inspection shows that the static stability of the lower stratosphere is nearly uniform for all storms, with $N \sim 0.022 \text{ s}^{-1}$. Analysis of the remaining warming dependencies for the mountain flow assumption is possible

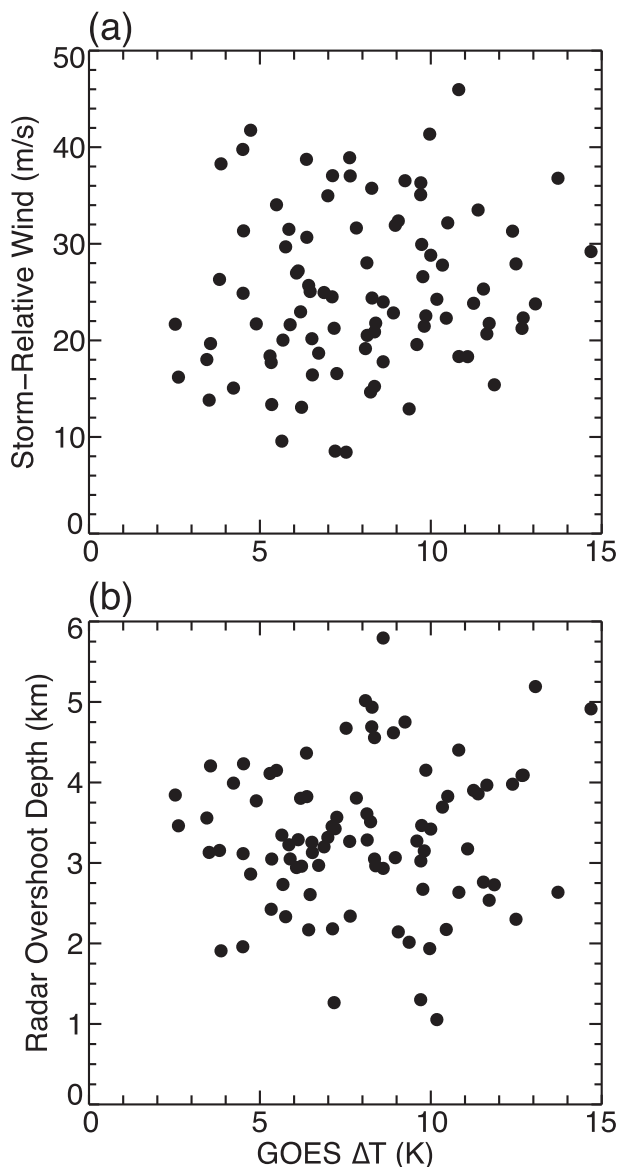


FIG. 12. For enhanced-V overshooting tops: (a) ERA-Interim environmental wind speed relative to radar-derived storm motion and (b) radar-derived relative altitude of overshooting to the neighboring anvil as a function of the along-apex minimum-to-maximum GOES IR temperature change.

given the observed characteristics of the overshoot and storm motion from radar. Figures 12a and 12b show storm-relative wind speed and the radar-observed depth of the overshoot relative to the surrounding anvil (a more conservative estimate than relative to the tropopause) as a function of the along-apex minimum-to-maximum IR temperature difference, respectively. Storm motion is determined by tracking of the maximum overshoot altitude from the radar composite over the analyzed time window (± 30 min of the IR measurement).

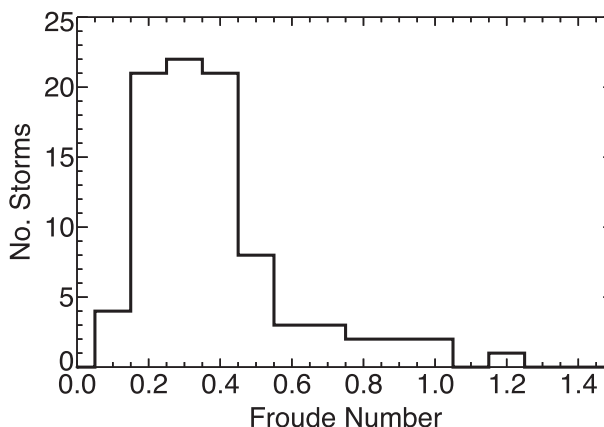


FIG. 13. Frequency distribution of the Froude number (Fr) for identified storms.

Both storm-relative wind and overshooting depth show no sensitivity to the magnitude of the warming. In addition to direct comparisons between the observed quantities, Fig. 13 shows a frequency distribution of estimates of the Froude number using the background static stability values from ERA-Interim and the radar storm characteristics from Fig. 12. The distribution of Fr shows a broad peak from 0.2 to 0.4, with only one storm exceeding the theoretical limit ($Fr = 1$) for flow over the overshoot rather than around it. Furthermore, considering the range of storm-relative wind speeds observed for the cases analyzed in this study ($10\text{--}40\text{ m s}^{-1}$) and assuming constant lower stratospheric stability similar to that outlined above, overshooting depths required to inhibit flow over the convective top (i.e., $Fr < 1$) follow a linear relationship from ~ 450 m at wind speeds of 10 m s^{-1} to ~ 1800 m at wind speeds of 40 m s^{-1} . These comparisons provide further support for the unlikely role of subsidence as a responsible mechanism for the formation of the enclosed warm anvil region.

4. Summary and discussion

A unique approach for the combination of volumetric reflectivity from individual radars into composite three-dimensional domains with high vertical resolution (1 km), described in detail in section 2d, has been introduced for mapping the horizontal and vertical extent of deep convective storms. These composite reflectivity fields are used to test the importance of various formation mechanisms for the enhanced-V IR satellite feature observed above tropopause-penetrating thunderstorms. For the 10-yr period from 2001 to 2010, 89 enhanced-V storms are found to have sufficient radar coverage within the NEXRAD WSR-88D network. The identified storms share common geographic,

annual, and temporal distributions with severe storms over the continental United States, in agreement with previous studies.

Cross sections through the apex of the enhanced V and in a coordinate relative to the maximum altitude of the storm illustrate the typical vertical extent of the overshooting top and the characteristic temperature change from the cold overshoot to the warm anvil region downstream (Fig. 10). Maximum relative altitudes of the 10 dBZ radar reflectivity surface are shown to be 2–5 km above the unperturbed environmental tropopause and at altitudes at or above the temperature maximum of a strong tropopause inversion layer (TIL). The coldest points of the corresponding IR temperatures nearly coincide with the radar overshooting top. The temperature gradient from the cold overshoot into the enclosed warm region of the downstream anvil is sharp, with maximum temperatures observed ~30 km downstream. On average, this cold-to-warm temperature change is observed to be about 6 K. This temperature change is comparable to cases observed by IR satellite instruments with similar horizontal resolution in previous studies. Recent studies with higher-resolution IR data show that this temperature change is often twice as large, due primarily to insufficient resolution of the coldest overshoot temperatures in the GOES data (e.g., Brunner et al. 2007). The along-apex sections also show that the warmest anvil temperatures do not correspond to reflectivity altitudes below the tropopause, suggesting that subsidence of the cloud below the tropopause is not a responsible mechanism for the development of an enclosed warm region.

Transverse cross-sections through the cold V branches and enclosed warm region of the enhanced V further shed light on the efficacy of the proposed formation mechanisms (see Fig. 11). The transverse cross sections clearly illustrate the presence of an enclosed warm region atop the anvil. Relative altitudes of the 10-dBZ radar reflectivity surface to the tropopause, however, reach a maximum within the warm region. This altitude peak is in disagreement with that expected from strong subsidence warming downstream of the overshooting top. In addition, altitudes of the 15- and 20-dBZ radar reflectivity surfaces show a similar transverse structure. Because IWC and radar reflectivity in the anvil region of storms are correlated, such an altitude structure in reflectivity illustrates that differences in IWC between the cold V branches and enclosed warm region are likely not responsible for the observed enhanced-V feature. An important caveat of these results, however, is that the minimum detectable signal of the WSR-88D data precludes direct observation of the cloud top, for which undetected variability in IWC could still play an important role.

Although the WSR-88D reflectivity serves as a good representation of the structure and extent of a storm, differences in the radar-observed and actual cloud top in the downstream anvil region could be significant and subsidence in the wake of the updraft could remain undetected. Assuming that lower-stratospheric flow over the updraft is similar to flow over a mountain, the expected relationships between the magnitude of the overshoot-to-anvil warming and both the overshooting depth and storm-relative wind were examined with the observations. No correlation was found between the observed warming and both storm parameters. In addition, only one of the storms exceeds the theoretical Froude number limit for the environmental air to travel over the overshoot, rather than around it, further suggesting the unlikely role of subsidence warming as a potential formation mechanism for the enhanced V. The lack of support for theoretical considerations, however, could in part be a result of neglecting perturbation pressure gradients, condensational effects on stability, and the likely inappropriate application of mountain theory to an overshooting convective top, which does not interact with the flow in the same way that terrain obstacles do (e.g., Smith 1990; Davies-Jones et al. 1994). Additional modeling studies of enhanced-V storms could provide detailed representations of the characteristic flow structure in the lower stratosphere and support for validating the unlikely role of subsidence as a potential formation mechanism.

The time interpolation for radar data used in this study could also introduce some uncertainty in the reflectivity field, which could affect the representation of the horizontal and vertical extent of convection. One important factor is the use of central scan times of each radar volume as a reference time for interpolation of the entire volume prior to three-dimensional compositing, while the observations for individual elevation angles take place over a much smaller time period than the entire volume (~5 min). In addition, despite frequent sampling, individual convective storms can travel several kilometers between the 5-min scan times, which can lead to underestimates of the interpolated reflectivity field. Although these sources of uncertainty are expected to be insignificant for the analyses in this study, improving the temporal interpolation technique and accounting for storm motion is an important consideration for three-dimensional compositing used in future studies.

The available observations do not enable the examination of stratospheric cirrus above the identified storms. Despite this limitation, analyses of the IR temperatures and radar reflectivity composites suggest that both subsidence and variable anvil IWC are unlikely responsible

mechanisms. The elimination of these mechanisms suggests that stratospheric cirrus are the most likely formation mechanism for the enhanced V. This finding is not surprising given the considerable amount of evidence of above-anvil cirrus in the literature. Further observations of both enhanced-V storms and other storm systems that exhibit similar cold-to-warm temperature couplets atop the anvil region are required to examine their relationship with stratospheric cirrus. Potential observational approaches include in situ measurements from high-altitude research aircraft and observations from remote systems capable of detecting the smaller cloud particles. In addition, the relative contributions of anvil lofting via gravity wave breaking and turbulent mixing of the overshoot summit to the occurrence of stratospheric cirrus requires further attention.

Stratospheric cirrus formation from turbulent mixing of convective overshoots or lofting of the adjacent anvil is capable of not only producing similar temperature features to the enhanced V but represents a potentially significant amount of troposphere-to-stratosphere transport. In particular, copious water vapor from the direct injection and evaporation of these clouds in the much drier stratosphere can have large impacts on radiation and climate (e.g., Forster and Shine 1999; Solomon et al. 2010). The enhanced-V storms identified in this study overshoot a midlatitude tropopause with a strong TIL, as evidenced by the radiosonde observations (Fig. 9b). The overshooting tops exceeded the altitude of the TIL temperature maximum by several kilometers. In the event stratospheric cirrus formed from turbulent mixing of the overshooting top with the background stratosphere, the warmer temperatures of the TIL could limit the return of the stratospheric cirrus cloud to the anvil top and troposphere. Although not shown, the mean IR temperature in the enclosed warm anvil region of the identified enhanced-V storms is nearly equivalent to the observed radiosonde TIL temperature maximum. The consistency between these observations may be related to the presence of stratospheric cirrus. In addition, the altitude of overshooting exceeds 380 K in potential temperature, which is taken to be the ceiling of the extratropical lower stratosphere (e.g., Hoskins 1991; Holton et al. 1995). Because the lower stratosphere is characterized by large-scale descent, convective injection of water vapor above 380 K could have larger impacts on the radiation budget of the stratosphere.

The frequency of tropopause-penetrating storms and associated transport in midlatitudes is not known and direct observations of convectively injected water vapor and other tropospheric trace gases are limited (e.g., Fischer et al. 2003; Hegglin et al. 2004). Because the potential for significant contribution to stratospheric

water vapor is large, further characterizations of the extent and frequency of convective overshooting are needed. The combination methods for high-resolution three-dimensional radar data introduced in this study provide a unique opportunity for accurately characterizing convective overshooting in midlatitudes over the continental United States. Radar data serve as an estimate of the true vertical extent of a storm that is not limited in space or time. Other available observations such as satellite-based imagery and lidar are limited in both space and time and often involve inference of the altitude of the storm from collocated meteorological analyses, which can introduce significant uncertainties. Climatological analysis of overshooting from the radar perspective for the study region in Fig. 3 is currently underway. In addition, similar studies of overshooting for organized convective systems are planned.

Acknowledgments. The author thanks the European Center for Medium-Range Weather Forecasting for providing the ERA-Interim data, which were obtained from the Research Data Archive (RDA) maintained by the Computational and Information Systems Laboratory (CISL) at the National Center for Atmospheric Research (NCAR). The original data are available from the RDA (<http://rda.ucar.edu>) in dataset number ds627.0. The author thanks the NASA CloudSat project for access to the Cloud Profiling Radar data, which were obtained from the CloudSat data processing center at Colorado State University (<http://www.cloudsat.cira.colostate.edu>). The author also thanks Matthew Kumjian, Scott Ellis, and Arthur Mizzi at NCAR for helpful discussions, and the Advanced Study Program (ASP) at NCAR for postdoctoral support.

REFERENCES

- Adler, R. F., and R. A. Mack, 1986: Thunderstorm cloud-top dynamics as inferred from satellite observations and a cloud top parcel model. *J. Atmos. Sci.*, **43**, 1945–1960.
- , D. D. Fenn, and D. A. Moore, 1981: Spiral feature observed at top of rotating thunderstorm. *Mon. Wea. Rev.*, **109**, 1124–1129.
- , M. J. Markus, D. D. Fenn, G. Szejwach, and W. E. Shenk, 1983: Thunderstorm top structure observed by aircraft overflights with an infrared radiometer. *J. Climate Appl. Meteor.*, **22**, 579–593.
- , —, and —, 1985: Detection of severe midwest thunderstorms using geosynchronous satellite data. *Mon. Wea. Rev.*, **113**, 769–781.
- Birner, T., 2006: Fine-scale structure of the extratropical tropopause. *J. Geophys. Res.*, **111**, D04104, doi:10.1029/2005JD006301.
- Brunner, J. C., S. A. Ackerman, A. S. Bachmeier, and R. M. Rabin, 2007: A quantitative analysis of the enhanced-V feature in relation to severe weather. *Wea. Forecasting*, **22**, 853–872.

- Crum, T. D., and R. L. Alberty, 1993: The WSR-88D and the WSR-88D operational support facility. *Bull. Amer. Meteor. Soc.*, **74**, 1669–1687.
- Davies-Jones, R., C. A. Doswell, and H. E. Brooks, 1994: Comments on “Initiation and evolution of updraft rotation within an incipient supercell thunderstorm.” *J. Atmos. Sci.*, **51**, 326–331.
- Dee, D. P., and Coauthors, 2011: The ERA-Interim reanalysis: Configuration and performance of the data assimilation system. *Quart. J. Roy. Meteor. Soc.*, **137**, 553–597, doi:10.1002/qj.828.
- Doswell, C. A., H. E. Brooks, and M. P. Kay, 2005: Climatological estimates of daily local nontornadic severe thunderstorm probability for the United States. *Wea. Forecasting*, **20**, 577–595.
- Doviak, R. J., and D. S. Zrnić, 1993: *Doppler Radar and Weather Observations*. 2nd ed. Dover Publications, 592 pp.
- Fischer, H., and Coauthors, 2003: Deep convective injection of boundary layer air into the lowermost stratosphere at mid-latitudes. *Atmos. Chem. Phys.*, **3**, 739–745.
- Forster, P. M. F., and K. P. Shine, 1999: Stratospheric water vapour changes as a possible contributor to observed stratospheric cooling. *Geophys. Res. Lett.*, **26**, 3309–3312.
- Fujita, T. T., 1982: Principle of stereoscopic height computations and their applications to stratospheric cirrus over severe thunderstorms. *J. Meteor. Soc. Japan*, **60**, 355–368.
- Heggin, M. I., and Coauthors, 2004: Tracing troposphere-to-stratosphere transport above a mid-latitude deep convective system. *Atmos. Chem. Phys.*, **4**, 741–756, doi:10.5194/acp-4-741-2004.
- Heymtsfield, G. M., and R. H. Blackmer, 1988: Satellite-observed characteristics of Midwest severe thunderstorm anvils. *Mon. Wea. Rev.*, **116**, 2200–2224.
- , R. H. Blackmer Jr., and S. Schotz, 1983a: Upper-level structure of Oklahoma tornadic storms on 2 May 1979. I: Radar and satellite observations. *J. Atmos. Sci.*, **40**, 1740–1755.
- , G. Szejwach, S. Schotz, and R. H. Blackmer Jr., 1983b: Upper-level structure of Oklahoma tornadic storms on 2 May 1979. II: Proposed explanation of “V” pattern and internal warm region in infrared observations. *J. Atmos. Sci.*, **40**, 1756–1767.
- , R. Fulton, and J. D. Spinhirne, 1991: Aircraft overflight measurements of midwest severe storms: Implications on geosynchronous satellite interpretations. *Mon. Wea. Rev.*, **119**, 436–456.
- Holton, J. R., P. H. Haynes, M. E. McIntyre, A. R. Douglass, and L. Pfister, 1995: Stratosphere-troposphere exchange. *Rev. Geophys.*, **33**, 403–439.
- Homeyer, C. R., K. P. Bowman, and L. L. Pan, 2010: Extratropical tropopause transition layer characteristics from high-resolution sounding data. *J. Geophys. Res.*, **115**, D13108, doi:10.1029/2009JD013664.
- Hoskins, B. J., 1991: Towards a PV-theta view of the general circulation. *Tellus*, **43**, 27–35.
- Houze, R. A., S. A. Rutledge, M. I. Biggerstaff, and B. F. Smull, 1989: Interpretation of doppler weather radar displays of midlatitude mesoscale convective systems. *Bull. Amer. Meteor. Soc.*, **70**, 608–619.
- Kelly, D. L., and J. T. Schaefer, 1985: Climatology of nontornadic severe thunderstorm events in the United States. *Mon. Wea. Rev.*, **113**, 1997–2014.
- Lakshmanan, V., T. Smith, K. Hondl, G. J. Stumpf, and A. Witt, 2006: A real-time, three-dimensional, rapidly updating, heterogeneous radar merger technique for reflectivity, velocity, and derived products. *Wea. Forecasting*, **22**, 802–823.
- Langston, C., J. Zhang, and K. Howard, 2007: Four-dimensional dynamic radar mosaic. *J. Atmos. Oceanic Technol.*, **24**, 776–790.
- Levizzani, V., and M. Setvák, 1996: Multispectral, high-resolution satellite observations of plumes on top of convective storms. *J. Atmos. Sci.*, **53**, 361–369.
- Lin, Y.-L., 1986: Calculation of airflow over an isolated heat source with application to the dynamics of v-shaped clouds. *J. Atmos. Sci.*, **43**, 2736–2751.
- Liu, C.-L., and A. J. Illingworth, 2000: Toward more accurate retrievals of ice water content from radar measurements of clouds. *J. Appl. Meteor.*, **39**, 1130–1146.
- Ludering, G., J. Trentmann, K. Hungershofer, M. Herzog, M. Fromm, and M. O. Andreae, 2007: Small-scale mixing processes enhancing troposphere-to-stratosphere transport by pyrocumulonimbus storms. *Atmos. Chem. Phys.*, **7**, 5945–5957.
- Mack, R. A., A. F. Hasler, and R. F. Adler, 1983: Thunderstorm cloud-top observations using satellite stereoscopy. *Mon. Wea. Rev.*, **111**, 1949–1964.
- McCann, D. W., 1983: The enhanced-V: A satellite observable severe storm signature. *Mon. Wea. Rev.*, **111**, 887–894.
- Menzel, W. P., and J. F. W. Purdom, 1994: Introducing GOES-I: The first of a new generation of geostationary operational environmental satellites. *Bull. Amer. Meteor. Soc.*, **75**, 757–781.
- Negri, A. J., 1982: Cloud-top structure of tornadic storms on 10 April 1979 from rapid scan and stereo satellite observations. *Bull. Amer. Meteor. Soc.*, **63**, 1151–1159.
- Office of the Federal Coordinator for Meteorology, cited 2005: Doppler radar meteorological observations, Part b: Doppler radar theory and meteorology. OFCM Rep. FCM-H11B-2005, 219 pp. [Available online at <http://www.ofcm.gov/fmh11/fmh11.htm>.]
- Ruzanski, E., and V. Chandrasekar, 2012: An investigation of the short-term predictability of precipitation using high-resolution composite radar observations. *J. Appl. Meteor. Climatol.*, **51**, 912–925.
- Sassen, K., 1987: Ice cloud content from radar reflectivity. *J. Climate Appl. Meteor.*, **26**, 1050–1053.
- Schlesinger, R. E., 1990: Overshooting thunderstorm cloud top dynamics as approximated by a linear Lagrangian parcel model with analytic exact solutions. *J. Atmos. Sci.*, **47**, 988–998.
- Setvák, M., and C. A. Doswell, 1991: The AVHRR channel-3 cloud-top reflectivity of convective storms. *Mon. Wea. Rev.*, **119**, 841–847.
- , and Coauthors, 2010: Satellite-observed cold-ring-shaped features atop deep convective clouds. *Atmos. Res.*, **97**, 80–96, doi:10.1016/j.atmosres.2010.03.009.
- , K. Bedka, D. T. Lindsey, A. Sokol, Z. Charvát, J. Štáštka, and P. K. Wang, 2013: A-Train observations of deep convective storm tops. *Atmos. Res.*, **123**, 229–248, doi:10.1016/j.atmosres.2012.06.020.
- Smith, R. B., 1990: Why can't stably stratified air rise over high ground? *Atmospheric Processes over Complex Terrain, Meteor. Monogr.*, No. 23, Amer. Meteor. Soc., 105–107.
- Solomon, S., K. H. Rosenlof, R. W. Portmann, J. S. Daniel, S. M. Davis, T. J. Sanford, and G.-K. Plattner, 2010: Contributions

- of stratospheric water vapor to decadal changes in the rate of global warming. *Science*, **327**, 1219–1223, doi:10.1126/science.1182488.
- Spinhirne, J. D., M. Z. Hansen, and J. Simpson, 1983: The structure and phase of cloud tops as observed by polarization lidar. *J. Climate Appl. Meteor.*, **22**, 1319–1331.
- Stephens, G. L., and Coauthors, 2002: The *CloudSat* mission and the A-Train: A new dimension of space-based observations of clouds and precipitation. *Bull. Amer. Meteor. Soc.*, **83**, 1771–1790.
- Trapp, R. J., and C. A. Doswell, 2000: Radar data objective analysis. *J. Atmos. Oceanic Technol.*, **17**, 105–120.
- Wang, P. K., 2003: Moisture plumes above thunderstorm anvils and their contributions to cross-tropopause transport of water vapor in midlatitudes. *J. Geophys. Res.*, **108**, 4194, doi:10.1029/2002JD002581.
- World Meteorological Organization, 1957: Meteorology—A three-dimensional science: Second session of the commission for aerology. *WMO Bull.*, **4**, 134–138.
- Zhang, J., K. Howard, and J. J. Gourley, 2005: Constructing three-dimensional multiple-radar reflectivity mosaics: Examples of convective storms and stratiform rain echoes. *J. Atmos. Oceanic Technol.*, **22**, 30–42.